Offline impact of transcranial focused ultrasound on cortical activation in primates

Lennart Verhagen[1,2,9*†], Cécile Gallea[3*], Davide Folloni[1,2], Charlotte Constans[4], Daria Jensen[1,2], Harry Ahnine[3], Léa Roumazeilles[1,2], Matthieu Santin[3], Bashir Ahmed[5], Stéphane Lehericy[3], Miriam Klein-Flügge[1,2], Kristine Krug[5], Rogier B Mars[2,6], Matthew FS Rushworth[1,2,8*], Pierre Pouget[7,8*], Jean-François Aubry[4,8*], Jérôme Sallet[1,2,8*†]

[1] Wellcome Centre for Integrative Neuroimaging (WIN), Department of Experimental Psychology, University of Oxford, Oxford, OX1 3SR, UK

[2] Wellcome Centre for Integrative Neuroimaging (WIN), Centre for Functional MRI of the Brain (FMRIB), Nuffield Department of Clinical Neurosciences, John Radcliffe Hospital, University of Oxford, Oxford, OX3 9DU, UK

[3] Institute du Cerveau et de la Moelle épinière (ICM), Centre for NeuroImaging Research (CENIR), Inserm U 1127, CNRS UMR 7225, Sorbonne Université, F-75013, Paris, France

[4] Institute Langevin, ESPCI Paris, PSL Research University, CNRS 7587, UMRS 979 INSERM, Sorbonne Université, Paris, France

[5] Department of Physiology, Anatomy, and Genetics, University of Oxford, Oxford, OX1 3PT, UK

[6] Donders Institute for Brain, Cognition and Behaviour, Radboud University Nijmegen, 6525 HR, Nijmegen, the Netherlands

[7] Institute du Cerveau et de la Moelle épinière (ICM), UMRS 975 INSERM, CNRS 7225, UMPC, Paris, France

[8] Senior author

[9] Lead Contact

* These authors contributed equally

† Correspondence

E-mail: lennart.verhagen@psy.ox.ac.uk, jerome.sallet@psy.ox.ac.uk

Twitter: @LennartVerhagen, @jerome_sallet

Address: Lennart Verhagen, Jérôme Sallet
Department of Experimental Psychology,
University of Oxford,
Tinsley Building,
Mansfield Road,
Oxford,
OX1 3SR, UK

Summary: 150 words
Overall length: 29,639 characters
Figures: 4 figures

Highlights

- Many studies of ultrasound neuromodulation focus on online effects in rodents.
- We use fMRI connectivity to investigate its offline impact in the primate brain.
- 40 s of ultrasound leads to a sustained, specific, reversible neural modulation.
- Ultrasound caused a sharpening of the stimulated region's connectivity profile.

In Brief

A new application of focused ultrasound safely modulates brain activation in primates for up to 2 hours after 40 seconds of stimulation. Ultrasound caused the stimulated area to interact more selectively with the rest of the brain.

Summary

To understand brain circuits it is necessary both to record and manipulate their activity. Despite increased availability of techniques for manipulating neural activity in rodents, manipulating neural activity in primates remains difficult. Here we show that a minimally invasive technique, transcranial focused ultrasound stimulation (TUS), induced offline changes to activity of circumscribed brain regions in the macaque. Applying TUS to the supplementary motor area or frontal polar cortex resulted in spatially specific patterns of activity change measurable with functional magnetic resonance imaging. In each case changes reflected each area's known network of interactions with the rest of the brain. Independent of these specific neural effects, TUS over these regions also induced widespread signal changes that might have a non-neuronal origin possibly mediated by the cerebral spinal fluid compartment. Although sustained for more than one hour beyond the 40s stimulation period, TUS effects were reversible and not associated with histological changes.

Introduction

In neuroscience, to understand brain circuits a two-pronged approach, entailing both recording and manipulating brain activity, is essential. In recent years, there has been extensive progress in this field, which was in part made possible by the availability of new technologies (Bestmann and Walsh, 2017; Dayan et al., 2013; Polanía et al., 2018). While techniques for transiently manipulating activity in rodents, such as optogenetics and chemogenetics (Khatoun et al., 2017; Sternson and Roth, 2014; Tang et al., 2018; Yizhar et al., 2011), are increasingly accessible and applied, techniques for manipulating activity in the primate brain are less widely available and remain accessible to comparatively few researchers in a limited number of research centers worldwide (Cicmil and Krug, 2015; Galvan et al., 2018). While successes have been achieved with some techniques, such as electrical microstimulation, these techniques have yet to prove their full potential, especially for impacting on cortical activity and behavior (Krug et al., 2015; Vanduffel, 2016).

Low intensity transcranial focused ultrasound stimulation (TUS) is a relatively new technique (Tufail et al., 2011; Yoo et al., 2011; Younan et al., 2013). Like transcranial magnetic stimulation (Dayan et al., 2013) and transcranial current stimulation (Polanía et al., 2018), TUS can be applied in the absence of a craniotomy. As such it has potential as a minimally invasive tool for transiently manipulating activity in the primate brain. In vitro recordings have identified several mechanisms by which ultrasound stimulation could affect neurons. It has been proposed that the sound pressure wave exerts a mechanical effect on neuronal activity through ion channel gating (Kubanek et al., 2018, 2016; Prieto et al., 2013). In the macaque, its application over the frontal eye field (FEF) affects the same aspects of oculomotor behavior that are compromised by FEF lesion, whilst leaving intact those aspects of oculomotor behavior that are unaffected by FEF lesion (Deffieux et al., 2013). Recent work has highlighted the possibility that for some stimulation protocols in rodents TUS interacts with neural activity through an auditory pathway (Guo et al., 2018; Sato et al., 2018). Importantly, this auditory effect is limited to the stimulation period and dissipates within 75 ms to 4 s. In summary, the impact that any stimulation protocol might have, will be a function of the animal model being used and the precise details of the ultrasound frequencies, pulse shape, and protocol.

Here we focused on the offline effects of TUS, investigating the impact of 40 s trains of TUS on measurements of neural activity provided by functional magnetic resonance imaging

(fMRI) up to 2 hours after stimulation. FMRI is one of the most widely used methods for estimating neural activity. Despite limitations in its spatial and temporal resolution, fMRI remains important because it is non-invasive and can often be used to provide information about activity throughout the whole brain. Rather than providing a direct measure of neural activity, however, it provides an estimate of how activity changes in tandem with sensory, cognitive, or motor events or with activity in another brain region. Typically, fMRI-measured activity in any given brain area is a function of activity in other brain areas especially those with which it is closely interconnected (Neubert et al., 2015; O'Reilly et al., 2013). Although many brain areas may share any given individual connection (for example both areas A and B may project to C), the overall pattern of connections of each area is unique (Passingham et al., 2002); as such, the overall pattern of connections therefore constitutes a "connectional fingerprint". As a result it is possible to use fMRI measurements of correlations in the blood oxygen level dependent (BOLD) signal across brain regions to estimate the connectivity fingerprints of a given brain area (Caspari et al., 2018; Ghahremani et al., 2017; Margulies et al., 2016, 2009; Mars et al., 2013; Sallet et al., 2013; Shen, 2015; Shen et al., 2015). This implies that activity in any given brain area is a function of the activity in the areas with which it is interconnected.

We exploited this feature of activity to examine the impact of TUS application to two brain regions in the frontal cortex: supplementary motor area (SMA; experiment 1) and frontal polar cortex (FPC; experiment 2; see fig S4 for details on TUS targeting). These regions have distinct anatomical and functional connections; SMA is most strongly coupled with the sensorimotor system, while the FPC interact primarily with the prefrontal cortex (Luppino et al., 2001; Petrides and Pandya, 2007; Sallet et al., 2013). This allows us to test the spatial and connectional specificity of TUS effects. In the control state, each area's activity is normally a function of the activity in the areas that constitute its connectional fingerprint. If this pattern is altered by TUS in a manner that is dependent on the location of the stimulation, then this will constitute evidence that TUS exerts a spatially selective effect on neural activity. The same three animals participated in experiments 1 and 2, and a control experiment conducted in the absence of TUS. We also validated the results of experiment 2 in a new set of three different animals (experiment 3).

Modulation of both SMA and FPC led to widespread signal changes in the 'cerebral spinal fluid' (CSF) compartment, independent of each area's connectional fingerprint.

Conversely, gray matter signal additionally revealed focal, area-specific effects of TUS. In each area, a region's activity pattern after TUS application was more a function of its own activity and that of strongly connected regions, but less a function of activity in more remote and weakly interconnected areas. Finally, in experiment 4 we demonstrate that TUS application had no observable impact on cortical microstructure apparent on histological examination. In summary, although TUS over dorsomedial frontal cortex leads to widespread BOLD signal enhancement, it also causes spatially specific sharpening of the stimulated region's connectivity profile in a reversible manner with high efficacy and reproducibility. The offline nature of these effects excludes the possibility that they originate from an auditory response.

Results

Experiment 1

Transcranial focused ultrasound stimulation of SMA induced spatially specific changes to SMA's connectivity profile, superimposed on more widespread signal changes. The specific changes are evident in fully processed resting-state fMRI data and will be described in detail below. However, first, we will report on minimally processed data that allow us to interrogate the global effects of TUS on blood-oxygen-level dependent signal (see Methods for full details). In these data, we observed that SMA stimulation induced widespread signal coupling compared to the control condition. This effect was not limited to the stimulation site but also present in remote regions. This can be illustrated by whole-brain functional connectivity seeded in a region away from the stimulation site, comparing between control and SMA conditions (for example, fig 1a-b illustrates the case of the posterior parietal operculum, POp). This effect can be quantified by considering the strength of local connections for every point in the cortex. It is then apparent that the changes induced by stimulation are global in nature (fig 1d). In general, following TUS, a region's connectivity profile could be predicted by considering its profile in the control condition and adding a spatially flat constant. This suggests an additional non-neuronal global signal contributes to many brain regions after TUS. In fact, the enhanced coupling was not limited to the gray matter, but also present strongly even in signal measured within the CSF, which includes some blood vessels, such as the superior sagittal sinus, close to the stimulation site and which might be directly affected by the TUS. A principal component analysis of the signal in the gray matter and CSF compartments revealed the main components explained significantly more variance following TUS compared to control (fig 1c; main effect of TUS: $F_{(1,9)}=30.6$, $p<0.001$; in gray matter: $F_{(1,4)}=10.7$, $p=0.031$; in CSF: $F_{(1,4)}=16.2$, $p=0.016$). Accordingly, we hypothesized that CSF signal components may explain the presence and enhancement of global signal observed following TUS over SMA (Verhagen, L., 2012). Indeed, including CSF components in a linear regression framework removed both the anatomically implausible global signal present in the control condition (fig 1a, e.g. the prefrontal cortex, encircled) and the global enhancement of signal coupling observed after TUS over SMA (fig 1e-f, e.g. primary sensorimotor cortex).

Importantly, regression of both white matter (WM) and CSF signal components revealed further TUS-induced functional connectivity changes that were spatially specific to the region stimulated. Building on conventional resting-state approaches (Behzadi et al., 2007; Bijsterbosch et al., 2018; Caballero-Gaudes and Reynolds, 2017; Verhagen, L., 2012), from here on we will report on the data after regressing out the contributions of the mean time course and first five principal components of the WM and CSF signals (see Methods for full details).

After accounting for global signal changes, we observed that TUS applied to SMA changed its coupling with the sensorimotor system, anterior and posterior cingulate, anterior temporal, inferior parietal, and prefrontal cortex (fig 2, left column). This can be seen on the whole brain functional connectivity maps for the SMA region highlighted by the dashed white circles on the left column of panels in figure 2 (compare panels a and b in fig 2). It is also apparent in the illustration of SMA's connectional fingerprint (fig 3a). The distance of the blue line from the center of the figure (and hence its proximity to the circumference of the figure) indicates the strength of activity correlation between SMA and each of the other brain areas indicated on the circumference in the control state. The red line shows that SMA's coupling is enhanced with proximal areas in the sensorimotor system but reduced in many long-range connections after SMA TUS (non-parametric permutation test, p=0.017). The primary motor cortex (M1), superior parietal lobe (SPL), and middle cingulate cortex (MCC) in the dorsomedial sensorimotor network have been reported to be closely connected with the SMA, whereas prefrontal regions on the dorsomedial (area 9m and FPC), dorsolateral (areas 9-46d and 8A), and ventromedial (area 11m) surface, and those in the temporal lobe (anterior superior temporal gyrus, aSTG; middle superior temporal sulcus, midSTS), and parietal sections of the `default mode network` (caudal inferior parietal lobule, IPLc; posterior parietal cortex, PCC) have been reported to be less closely connected with the SMA (Dum and Strick, 2005; Geyer et al., 2000; Strick et al., 1998). TUS increased coupling between the stimulated area and proximal areas normally closely connected with it while, at the same time, decreasing coupling between the stimulated area and many areas normally less closely connected with it.

These specific effects of TUS were sustained over the duration of our experiment, lasting up to 2 hours (fig S3). Disruptive effects of TUS on long-range coupling were especially prominent immediately following the end of TUS application (fig S3D), and gradually reduced

towards the end of our recording session (fig S3F). Enhancing effects of TUS on SMA's coupling with proximal and strongly connected areas had a delayed appearance, arising well after the TUS had ended (more than 1 hour, fig S3E), but again decreasing towards the end of the recording session.

Experiment 2

In minimally processed data FPC stimulation again led to widespread enhanced signal coupling compared to the control condition (fig S1). Although the effect was not as strong as that seen after SMA TUS, this finding again suggests that TUS may produce widespread changes that are non-neuronal in origin. Similarly, regressing out CSF components (over and above WM components) strongly reduced the contribution of the global signal, but left spatially specific changes intact (fig 2, right column, compare panels d and f). In comparison to the control condition FPC stimulation induced an enhancement in short-range connectivity between FPC and adjacent dorsomedial and lateral prefrontal cortex with which it is particularly strongly connected (areas 9m and 9-46d). In addition, a similar effect was seen in more distant regions with which it is also strongly connected – the midSTS, IPLc and PCC, together comprising temporal and parietal segments of the primate 'default mode network' (Petrides and Pandya, 2007). By contrast, there was reduced coupling with other areas in prefrontal cortex, including ventromedial (area 14m), subgenual cingulate (area 25), and lateral orbitofrontal cortex (area 47-12o). These are all areas that FPC is connected to but less strongly (Petrides and Pandya, 2007). Finally, TUS applied to FPC also led to a change in long-range connectivity between FPC and several motor association regions with which it is not directly connected, especially those in the ventrolateral parieto-frontal sensorimotor network (areas PF and F4; Petrides and Pandya, 2007). In the control state, the activity in FPC and these sensorimotor association areas is negatively or anti-correlated, but this anti-correlation was reduced by FPC TUS. These results are apparent in the whole brain functional connectivity maps for the FPC region highlighted by the dashed white circle on right column of panels in figure 2 (compare panels d and f in fig 2). It is also apparent in the illustration of FPC's connectional fingerprint (fig 3b). Here the blue line indicates the strength of activity correlation between FPC and each of the other brain areas indicated on the circumference in

the control state. The yellow line shows that FPC's coupling with each area is changed after FPC TUS (non-parametric permutation test, p = 0.027).

Comparing experiments 1 and 2

Because TUS induced global coupling changes (fig 1), it is important to test the claim that it also induces spatially specific effects by directly comparing these effects between stimulation sites. Although FPC TUS significantly altered FPC functional connectivity, it had comparatively little impact on SMA's pattern of functional connectivity; there was no difference in SMA's functional connectivity between the control state and after FPC TUS (non-parametric permutation test, p = 0.231; whole-brain map in fig 2c and yellow line in connectivity fingerprint in fig 3a). Importantly, the effects of TUS over SMA on SMA's connectivity were significantly dissociable from the effects of FPC TUS (non-parametric permutation test, p = 0.041). Similarly, SMA TUS had some but comparatively little impact on FPC's pattern of functional connectivity (non-parametric permutation tests, SMA <> control, p = 0.047; SMA <> FPC, p = 0.028; whole-brain map in fig 2e and red line in connectivity fingerprint in fig 3b). In fact, the most prominent changes in each area's connectional fingerprint that were induced by stimulation of the other area were the disruption of functional connectivity between FPC and sensorimotor areas when SMA was stimulated (fig 2e, encircled). This one anomalous result may have occurred because FPC has no direct monosynaptic connections with these sensorimotor areas (Petrides and Pandya, 2007) and so its functional coupling with these areas is likely to be mediated by areas such as SMA and the areas that surround it such as the pre-supplementary motor area and the cingulate motor areas (Bates and Goldman-Rakic, 1993; Lu et al., 1994). In summary, the effects of TUS in different frontal regions were dissociable.

Experiment 3

We investigated the reproducibility of TUS effects by examining the impact of TUS to FPC in three additional individuals (fig S1, bottom row; fig S2). TUS had the same effects as seen in experiment 2. We note that while the coupling-enhancing effects of TUS were especially well matched between the two experiments, the disruptive effects of TUS were less prominent in experiment 3.

Experiment 4

Distinct ultrasound stimulation protocols to those used here have been shown to induce thermal lesions or hemorrhage following cavitation (Elias et al., 2013; Xu et al., 2015; Zhang et al., 2015). Despite the fact that trains of TUS induced sustained changes in the post-stimulation period in experiments 1 and 2, no structural changes remotely resembling those seen with different ultrasound protocols were visible in histological analyses of three macaques following pre-SMA TUS (fig 4).

Thermal modelling

To quantify potential TUS induced temperature changes in the monkey brain we simulated the thermal effect of focused ultrasound protocol as used in this study. We simulated the ultrasound acoustic wave propagation through a 3mm thick skull. Given that the skull is more acoustically absorbing than soft tissue, the highest thermal increase is located in the skull itself, estimated by the simulation to be 2.8°C. Given an approximate 0.5 mm thickness of the dura (Galashan et al., 2011) the maximum temperature below the dura was 38.0°C. The maximal thermal increase at the geometrical focus of the sonic transducer was less than 0.2 °C (fig S4).

Discussion

Each brain area's unique contribution to cognition and behavior is thought to be strongly shaped by how activity in each area is a function of a unique fingerprint of interconnected areas (Passingham et al., 2002). In this study we found that each area's connectional fingerprint was significantly changed by transcranial focused ultrasound stimulation (TUS), but only when it was applied to that area itself (figs 2, 3). The changes observed might be summarized as a sharpening of the normal pattern; activity coupling with strongly interconnected areas, which are often nearby, was increased but activity coupling with less strongly connected regions was reduced. Such changes in connectional fingerprints might constitute the mechanism by which TUS is able to induce regionally specific patterns of behavioral change when applied in awake behaving animals (Deffieux et al., 2013; Fouragnan et al., 2018). The pattern of inputs each area receives from other areas and the influence it wields over other areas are a major determinant of its function and here we have shown that this pattern is altered by TUS. TUS may therefore provide a relatively straightforward method for transient manipulation of specific components of neural circuits in the primate brain. This may be important for investigating primate brain areas when homologues in non-primate species, such as rodents, are non-existent or disputed (Preuss, 1995; Wise, 2008).

In experiments 1 and 2 we found that TUS application produced different effects when applied to different brain regions: the SMA, a part of motor association cortex and FPC a part of granular prefrontal cortex (figs 1, 2). However, in each case the TUS effects were prominent within the connectional fingerprint of the area stimulated. The connectional fingerprints of SMA and FPC are distinct (Johansen-Berg et al., 2004; Neubert et al., 2014; Sallet et al., 2013). The effects of TUS are thus regionally specific.

Our results confirm that TUS can be used as a neuromodulatory technique that allows one to non-invasively target cortical and subcortical brain areas with superior spatial specificity and depth of stimulation (Folloni et al., 2018), compared to other transcranial stimulation approaches (e.g., TMS, tCS; Bestmann and Walsh, 2017; Dayan et al., 2013; Polanía et al., 2018). Recently it has been reported that some online TUS protocols in rodents induce neural changes as an indirect consequence of the auditory stimulation they entail (Guo et al., 2018; Sato et al., 2018). The spatially specific effects that we observed after TUS cannot, however, be attributed to any common auditory impact that occurs at the time of stimulation.

Moreover, in order to avoid both the confounding effect associated with the sound of TUS and interference of the ultrasonic wave field with fMRI measurement, we opted for an offline stimulation protocol. Stimulation was a 40 s train that typically ended at least 20 minutes before the fMRI data acquisition period. The sustained nature of the train and other features of the stimulation pulses may make the protocol used here more effective for neuromodulation, while ensuring the thermal modulation of the cortex remains limited (< 0.6 °C, fig S4) and below the thermal effects observed with some protocols in rodents (for a review, see Constans et al., 2018).

In experiment 3 we found that TUS had reproducible effects. When TUS was applied to FPC in three other individuals, it induced spatially specific effects similar to those seen in experiment 2.

The effect of the stimulation protocol used here is sustained and lasted over much of the two-hour period we investigated. At least when stimulation is delivered in the 40 s trains employed here, the effects are more extended than other techniques commonly used for transient disruption of cortical activity such as TMS (Huang et al., 2005; O'Shea et al., 2007; Zimmermann et al., 2016). Care should therefore be taken in using the technique in human cognitive neuroscience experiments; TUS effects may continue beyond the short periods that participants typically spend within the laboratory. It may therefore be important to carefully characterize the time course of TUS effects in animal models before their use with human participants.

In addition to the spatially specific effects of TUS we also observed changes in the BOLD signal that were not specific to the area stimulated. Although similar effects were seen each time either the SMA or FPC was stimulated the effect was generally more pronounced after SMA stimulation than after FPC stimulation. Our preliminary results from TUS of other brain areas suggest that these spatially non-specific effects may be even smaller when TUS is applied elsewhere (Folloni et al., 2018). While the precise origin of the non-specific effects was difficult to determine it is possible that they may result from a direct vascular effect of TUS; the sagittal sinus is close to the SMA region that we targeted. The presence of such non-specific effects again underlines the need for care in translating the technique to humans. In addition, they underline the need for comparing the behavioral effects of TUS not just with a non-stimulation sham condition but with TUS application to another control brain region. The

absence of marked histological changes in experiment 4, however, provides one important safety benchmark.

Combining TUS and fMRI is a promising approach to overcome the restrictions of each of the individual techniques. Here we have shown that TUS has a detectable offline and sustained impact on the distinctive network of connectivity associated with the stimulated brain region – the connectional fingerprint. A brain region's interactions with other regions – its unique connectional fingerprint or specific pattern of inputs and outputs – are an important determinant of its functional role. The current results are therefore consistent with TUS application exerting regionally specific effects on behavior (Deffieux et al., 2013; Fouragnan et al., 2018). The fact that fMRI allows the effects of TUS to be studied with a high spatial resolution suggests TUS-fMRI combination has the potential to become a powerful neuroscientific tool.

Acknowledgements

We would like to thank Greg Daubney for his assistance with the histological preparation and analysis, and Dr. Constantin Coussios and Dr. Robin Cleveland for their technical support. Funding for this research was provided by a Wellcome Trust Henry Dale fellowship (105651/Z/14/Z), Wellcome Trust Senior Investigator Award (WT100973AIA), MRC programme grant (MR/P024955/1), MRC programme grant (G0902373), Wellcome Trust UK Grant (105238/Z/14/Z), Wellcome Trust Sir Henry Wellcome fellowship (103184/Z/13/Z), BBRSC grant (BB/N019814/1), NWO grant (452-13-015), The Wellcome Centre for Integrative Neuroimaging (203139/Z/16/Z), Bettencourt Schueller Foundation, and the Agence Nationale de la Recherche under the Future Investments program (ANR-10-EQPX-15).

Contributions

Conceptualization: PP, JFA, and JS; Methodology: LV, CC, MFSR, PP, JFA, JS; Data acquisition: DF, CC, HA, BA, MS, LR, KK, PP, JFA, and JS; Analysis: LV, CG, DF, CC, DJ, MFSR, JFA, and JS; Software: LV, CC, MKF, RBM, and JFA; Resources: SL, KK, MFSR, PP, JFA, and JS. Writing – original draft: LV, MFSR. Writing – editing: LV, CG, DF, KK, MFSR, PP, JFA, and JS. Visualization: LV, JF, JS. Supervision: LS, MFSR, PP, JFA, and JS. Funding: MFSR, PP, JFA, and JS.

Declaration of Interests

The authors have no competing interests to declare.

References

Andersson, J.L.R., Jenkinson, M., Smith, S., 2007. Non-linear registration aka Spatial normalisation - FMRIB Technial Report TR07JA2.

Aubry, J.-F., Tanter, M., Pernot, M., Thomas, J.-L., Fink, M., 2003. Experimental demonstration of noninvasive transskull adaptive focusing based on prior computed tomography scans. J. Acoust. Soc. Am. 113, 84–93. https://doi.org/10.1121/1.1529663

Bates, J.F., Goldman-Rakic, P.S., 1993. Prefrontal connections of medial motor areas in the rhesus monkey. J. Comp. Neurol. 336, 211–228. https://doi.org/10.1002/cne.903360205

Behzadi, Y., Restom, K., Liau, J., Liu, T.T., 2007. A component based noise correction method (CompCor) for BOLD and perfusion based fMRI. NeuroImage 37, 90–101. https://doi.org/10.1016/j.neuroimage.2007.04.042

Bestmann, S., Walsh, V., 2017. Transcranial electrical stimulation. Curr. Biol. 27, R1258–R1262. https://doi.org/10.1016/j.cub.2017.11.001

Bijsterbosch, J.D., Woolrich, M.W., Glasser, M.F., Robinson, E.C., Beckmann, C.F., Van Essen, D.C., Harrison, S.J., Smith, S.M., 2018. The relationship between spatial configuration and functional connectivity of brain regions. eLife 7, e32992. https://doi.org/10.7554/eLife.32992

Caballero-Gaudes, C., Reynolds, R.C., 2017. Methods for cleaning the BOLD fMRI signal. NeuroImage, Cleaning up the fMRI time series: Mitigating noise with advanced acquisition and correction strategies 154, 128–149. https://doi.org/10.1016/j.neuroimage.2016.12.018

Caspari, N., Arsenault, J.T., Vandenberghe, R., Vanduffel, W., 2018. Functional Similarity of Medial Superior Parietal Areas for Shift-Selective Attention Signals in Humans and Monkeys. Cereb. Cortex 28, 2085–2099. https://doi.org/10.1093/cercor/bhx114

Cicmil, N., Krug, K., 2015. Playing the electric light orchestra—how electrical stimulation of visual cortex elucidates the neural basis of perception. Phil Trans R Soc B 370, 20140206. https://doi.org/10.1098/rstb.2014.0206

Constans, C., Deffieux, T., Pouget, P., Tanter, M., Aubry, J.F., 2017. A 200-1380-kHz Quadrifrequency Focused Ultrasound Transducer for Neurostimulation in Rodents

and Primates: Transcranial In Vitro Calibration and Numerical Study of the Influence of Skull Cavity. IEEE Trans. Ultrason. Ferroelectr. Freq. Control 64, 717–724. https://doi.org/10.1109/TUFFC.2017.2651648

Constans, C., Mateo, P., Tanter, M., Aubry, J.-F., 2018. Potential impact of thermal effects during ultrasonic neurostimulation: retrospective numerical estimation of temperature elevation in seven rodent setups. Phys. Med. Biol. 63, 025003. https://doi.org/10.1088/1361-6560/aaa15c

Cox, B.T., Kara, S., Arridge, S.R., Beard, P.C., 2007. k-space propagation models for acoustically heterogeneous media: Application to biomedical photoacoustics. J. Acoust. Soc. Am. 121, 3453–3464. https://doi.org/10.1121/1.2717409

Dayan, E., Censor, N., Buch, E.R., Sandrini, M., Cohen, L.G., 2013. Noninvasive brain stimulation: from physiology to network dynamics and back. Nat. Neurosci. 16, 838–844. https://doi.org/10.1038/nn.3422

Deffieux, T., Younan, Y., Wattiez, N., Tanter, M., Pouget, P., Aubry, J.-F., 2013. Low-Intensity Focused Ultrasound Modulates Monkey Visuomotor Behavior. Curr. Biol. 23, 2430–2433. https://doi.org/10.1016/j.cub.2013.10.029

Duck, F.A., 2013. Physical Properties of Tissues: A Comprehensive Reference Book. Academic Press.

Dum, R.P., Strick, P.L., 2005. Frontal Lobe Inputs to the Digit Representations of the Motor Areas on the Lateral Surface of the Hemisphere. J. Neurosci. 25, 1375–1386. https://doi.org/10.1523/JNEUROSCI.3902-04.2005

Elias, W.J., Khaled, M., Hilliard, J.D., Aubry, J.-F., Frysinger, R.C., Sheehan, J.P., Wintermark, M., Lopes, M.B., 2013. A magnetic resonance imaging, histological, and dose modeling comparison of focused ultrasound, radiofrequency, and Gamma Knife radiosurgery lesions in swine thalamus. J. Neurosurg. 119, 307–317. https://doi.org/10.3171/2013.5.JNS122327

Folloni, D., Verhagen, L., Mars, R.B., Fouragnan, E., Aubry, J.-F., Rushworth, M.F.S., Sallet, J., 2018. Manipulation of activity in deep structures of the primate brain using transcranial fo-cused ultrasound stimulation. bioRxiv.

Fouragnan, E., Chau, B.K.H., Folloni, D., Kolling, N., Verhagen, L., Klein-Flügge, M., Tankelevitch, L., Papageorgiou, G.K., Aubry, J.-F., Sallet, J., Rushworth, M.F.S., 2018.

The macaque anterior cingulate cortex translates counterfactual choice value into actual behavioral change. bioRxiv.

Galashan, F.O., Rempel, H.C., Meyer, A., Gruber-Dujardin, E., Kreiter, A.K., Wegener, D., 2011. A new type of recording chamber with an easy-to-exchange microdrive array for chronic recordings in macaque monkeys. J. Neurophysiol. 105, 3092–3105. https://doi.org/10.1152/jn.00508.2010

Galvan, A., Caiola, M.J., Albaugh, D.L., 2018. Advances in optogenetic and chemogenetic methods to study brain circuits in non-human primates. J. Neural Transm. 125, 547–563. https://doi.org/10.1007/s00702-017-1697-8

Geyer, S., Matelli, M., Luppino, G., Zilles, K., 2000. Functional neuroanatomy of the primate isocortical motor system. Anat. Embryol. (Berl.) 202, 443–474.

Ghahremani, M., Hutchison, R.M., Menon, R.S., Everling, S., 2017. Frontoparietal Functional Connectivity in the Common Marmoset. Cereb. Cortex 27, 3890–3905. https://doi.org/10.1093/cercor/bhw198

Glasser, M.F., Sotiropoulos, S.N., Wilson, J.A., Coalson, T.S., Fischl, B., Andersson, J.L., Xu, J., Jbabdi, S., Webster, M., Polimeni, J.R., Van Essen, D.C., Jenkinson, M., 2013. The minimal preprocessing pipelines for the Human Connectome Project. NeuroImage, Mapping the Connectome 80, 105–124. https://doi.org/10.1016/j.neuroimage.2013.04.127

Goss, S.A., Frizzell, L.A., Dunn, F., 1979. Ultrasonic absorption and attenuation in mammalian tissues. Ultrasound Med. Biol. 5, 181–186. https://doi.org/10.1016/0301-5629(79)90086-3

Guo, H., Hamilton, M., Offutt, S.J., Gloeckner, C.D., Li, T., Kim, Y., Legon, W., Alford, J.K., Lim, H.H., 2018. Ultrasound Produces Extensive Brain Activation via a Cochlear Pathway. Neuron. https://doi.org/10.1016/j.neuron.2018.04.036

Huang, Y.-Z., Edwards, M.J., Rounis, E., Bhatia, K.P., Rothwell, J.C., 2005. Theta Burst Stimulation of the Human Motor Cortex. Neuron 45, 201–206. https://doi.org/10.1016/j.neuron.2004.12.033

Jenkinson, M., Bannister, P., Brady, M., Smith, S., 2002. Improved Optimization for the Robust and Accurate Linear Registration and Motion Correction of Brain Images. NeuroImage 17, 825–841. https://doi.org/10.1006/nimg.2002.1132

Jenkinson, M., Beckmann, C.F., Behrens, T.E.J., Woolrich, M.W., Smith, S.M., 2012. FSL. NeuroImage, 20 YEARS OF fMRI 62, 782–790. https://doi.org/10.1016/j.neuroimage.2011.09.015

Jenkinson, M., Smith, S., 2001. A global optimisation method for robust affine registration of brain images. Med. Image Anal. 5, 143–156. https://doi.org/10.1016/S1361-8415(01)00036-6

Johansen-Berg, H., Behrens, T.E.J., Robson, M.D., Drobnjak, I., Rushworth, M.F.S., Brady, J.M., Smith, S.M., Higham, D.J., Matthews, P.M., 2004. Changes in connectivity profiles define functionally distinct regions in human medial frontal cortex. Proc. Natl. Acad. Sci. 101, 13335–13340. https://doi.org/10.1073/pnas.0403743101

Khatoun, A., Asamoah, B., Laughlin, M.M., 2017. Simultaneously Excitatory and Inhibitory Effects of Transcranial Alternating Current Stimulation Revealed Using Selective Pulse-Train Stimulation in the Rat Motor Cortex. J. Neurosci. 37, 9389–9402. https://doi.org/10.1523/JNEUROSCI.1390-17.2017

Krug, K., Salzman, C.D., Waddell, S., 2015. Understanding the brain by controlling neural activity. Phil Trans R Soc B 370, 20140201. https://doi.org/10.1098/rstb.2014.0201

Kubanek, J., Shi, J., Marsh, J., Chen, D., Deng, C., Cui, J., 2016. Ultrasound modulates ion channel currents. Sci. Rep. 6, 24170. https://doi.org/10.1038/srep24170

Kubanek, J., Shukla, P., Das, A., Baccus, S.A., Goodman, M.B., 2018. Ultrasound Elicits Behavioral Responses through Mechanical Effects on Neurons and Ion Channels in a Simple Nervous System. J. Neurosci. 38, 3081–3091. https://doi.org/10.1523/JNEUROSCI.1458-17.2018

Lu, M.-T., Preston, J.B., Strick, P.L., 1994. Interconnections between the prefrontal cortex and the premotor areas in the frontal lobe. J. Comp. Neurol. 341, 375–392. https://doi.org/10.1002/cne.903410308

Luppino, G., Calzavara, R., Rozzi, S., Matelli, M., 2001. Projections from the superior temporal sulcus to the agranular frontal cortex in the macaque. Eur. J. Neurosci. 14, 1035–1040. https://doi.org/10.1046/j.0953-816x.2001.01734.x

Margulies, D.S., Ghosh, S.S., Goulas, A., Falkiewicz, M., Huntenburg, J.M., Langs, G., Bezgin, G., Eickhoff, S.B., Castellanos, F.X., Petrides, M., Jefferies, E., Smallwood, J., 2016. Situating the default-mode network along a principal gradient of macroscale cortical

organization. Proc. Natl. Acad. Sci. 113, 12574–12579. https://doi.org/10.1073/pnas.1608282113

Margulies, D.S., Vincent, J.L., Kelly, C., Lohmann, G., Uddin, L.Q., Biswal, B.B., Villringer, A., Castellanos, F.X., Milham, M.P., Petrides, M., 2009. Precuneus shares intrinsic functional architecture in humans and monkeys. Proc. Natl. Acad. Sci. 106, 20069–20074. https://doi.org/10.1073/pnas.0905314106

Mars, R.B., Jbabdi, S., Sallet, J., O'Reilly, J.X., Croxson, P.L., Olivier, E., Noonan, M.P., Bergmann, C., Mitchell, A.S., Baxter, M.G., Behrens, T.E.J., Johansen-Berg, H., Tomassini, V., Miller, K.L., Rushworth, M.F.S., 2011. Diffusion-Weighted Imaging Tractography-Based Parcellation of the Human Parietal Cortex and Comparison with Human and Macaque Resting-State Functional Connectivity. J. Neurosci. 31, 4087–4100. https://doi.org/10.1523/JNEUROSCI.5102-10.2011

Mars, R.B., Sallet, J., Neubert, F.-X., Rushworth, M.F.S., 2013. Connectivity profiles reveal the relationship between brain areas for social cognition in human and monkey temporoparietal cortex. Proc. Natl. Acad. Sci. 110, 10806–10811. https://doi.org/10.1073/pnas.1302956110

Mars, R.B., Verhagen, L., Gladwin, T.E., Neubert, F.-X., Sallet, J., Rushworth, M.F.S., 2016. Comparing brains by matching connectivity profiles. Neurosci. Biobehav. Rev. 60, 90–97. https://doi.org/10.1016/j.neubiorev.2015.10.008

McLaren, D.G., Kosmatka, K.J., Oakes, T.R., Kroenke, C.D., Kohama, S.G., Matochik, J.A., Ingram, D.K., Johnson, S.C., 2009. A population-average MRI-based atlas collection of the rhesus macaque. NeuroImage 45, 52–59. https://doi.org/10.1016/j.neuroimage.2008.10.058

Neubert, F.-X., Mars, R.B., Sallet, J., Rushworth, M.F.S., 2015. Connectivity reveals relationship of brain areas for reward-guided learning and decision making in human and monkey frontal cortex. Proc. Natl. Acad. Sci. 112, E2695–E2704. https://doi.org/10.1073/pnas.1410767112

Neubert, F.-X., Mars, R.B., Thomas, A.G., Sallet, J., Rushworth, M.F.S., 2014. Comparison of Human Ventral Frontal Cortex Areas for Cognitive Control and Language with Areas in Monkey Frontal Cortex. Neuron 81, 700–713. https://doi.org/10.1016/j.neuron.2013.11.012

O'Reilly, J.X., Croxson, P.L., Jbabdi, S., Sallet, J., Noonan, M.P., Mars, R.B., Browning, P.G.F., Wilson, C.R.E., Mitchell, A.S., Miller, K.L., Rushworth, M.F.S., Baxter, M.G., 2013. Causal effect of disconnection lesions on interhemispheric functional connectivity in rhesus monkeys. Proc. Natl. Acad. Sci. 110, 13982–13987. https://doi.org/10.1073/pnas.1305062110

O'Shea, J., Johansen-Berg, H., Trief, D., Göbel, S., Rushworth, M.F.S., 2007. Functionally Specific Reorganization in Human Premotor Cortex. Neuron 54, 479–490. https://doi.org/10.1016/j.neuron.2007.04.021

Passingham, R.E., Stephan, K.E., Kötter, R., 2002. The anatomical basis of functional localization in the cortex. Nat. Rev. Neurosci. 3, 606–616. https://doi.org/10.1038/nrn893

Pennes, H.H., 1948. Analysis of Tissue and Arterial Blood Temperatures in the Resting Human Forearm. J. Appl. Physiol. 1, 93–122. https://doi.org/10.1152/jappl.1948.1.2.93

Petrides, M., Pandya, D.N., 2007. Efferent Association Pathways from the Rostral Prefrontal Cortex in the Macaque Monkey. J. Neurosci. 27, 11573–11586. https://doi.org/10.1523/JNEUROSCI.2419-07.2007

Pinton, G., Aubry, J.-F., Bossy, E., Muller, M., Pernot, M., Tanter, M., 2012. Attenuation, scattering, and absorption of ultrasound in the skull bone. Med. Phys. 39, 299–307. https://doi.org/10.1118/1.3668316

Polanía, R., Nitsche, M.A., Ruff, C.C., 2018. Studying and modifying brain function with non-invasive brain stimulation. Nat. Neurosci. 21, 174–187. https://doi.org/10.1038/s41593-017-0054-4

Preuss, T.M., 1995. Do rats have prefrontal cortex? The rose-woolsey-akert program reconsidered. J. Cogn. Neurosci. 7, 1–24. https://doi.org/10.1162/jocn.1995.7.1.1

Prieto, M.L., Oralkan, Ö., Khuri-Yakub, B.T., Maduke, M.C., 2013. Dynamic Response of Model Lipid Membranes to Ultrasonic Radiation Force. PLoS ONE 8. https://doi.org/10.1371/journal.pone.0077115

Pulkkinen, A., Huang, Y., Song, J., Hynynen, K., 2011. Simulations and measurements of transcranial low-frequency ultrasound therapy: skull-base heating and effective area of treatment. Phys. Med. Biol. 56, 4661. https://doi.org/10.1088/0031-9155/56/15/003

Reveley, C., Gruslys, A., Ye, F.Q., Glen, D., Samaha, J., E. Russ, B., Saad, Z., K. Seth, A., Leopold, D.A., Saleem, K.S., 2017. Three-Dimensional Digital Template Atlas of the Macaque Brain. Cereb. Cortex 27, 4463–4477. https://doi.org/10.1093/cercor/bhw248

Sallet, J., Mars, R.B., Noonan, M.P., Neubert, F.-X., Jbabdi, S., O'Reilly, J.X., Filippini, N., Thomas, A.G., Rushworth, M.F., 2013. The Organization of Dorsal Frontal Cortex in Humans and Macaques. J. Neurosci. 33, 12255–12274. https://doi.org/10.1523/JNEUROSCI.5108-12.2013

Sato, T., Shapiro, M.G., Tsao, D.Y., 2018. Ultrasonic Neuromodulation Causes Widespread Cortical Activation via an Indirect Auditory Mechanism. Neuron. https://doi.org/10.1016/j.neuron.2018.05.009

Shen, H.H., 2015. Core Concept: Resting-state connectivity. Proc. Natl. Acad. Sci. 112, 14115–14116. https://doi.org/10.1073/pnas.1518785112

Shen, K., Hutchison, R.M., Bezgin, G., Everling, S., McIntosh, A.R., 2015. Network Structure Shapes Spontaneous Functional Connectivity Dynamics. J. Neurosci. 35, 5579–5588. https://doi.org/10.1523/JNEUROSCI.4903-14.2015

Smith, S.M., 2002. Fast robust automated brain extraction. Hum. Brain Mapp. 17, 143–155. https://doi.org/10.1002/hbm.10062

Smith, S.M., Hyvärinen, A., Varoquaux, G., Miller, K.L., Beckmann, C.F., 2014. Group-PCA for very large fMRI datasets. NeuroImage 101, 738–749. https://doi.org/10.1016/j.neuroimage.2014.07.051

Sternson, S.M., Roth, B.L., 2014. Chemogenetic Tools to Interrogate Brain Functions. Annu. Rev. Neurosci. 37, 387–407. https://doi.org/10.1146/annurev-neuro-071013-014048

Strick, P.L., Dum, R.P., Picard, N., 1998. Motor areas on the medial wall of the hemisphere. Novartis Found. Symp. 218, 64–75; discussion 75-80, 104–108.

Tang, A.D., Bennett, W., Hadrill, C., Collins, J., Fulopova, B., Wills, K., Bindoff, A., Puri, R., Garry, M.I., Hinder, M.R., Summers, J.J., Rodger, J., Canty, A.J., 2018. Low intensity repetitive transcranial magnetic stimulation modulates skilled motor learning in adult mice. Sci. Rep. 8, 4016. https://doi.org/10.1038/s41598-018-22385-8

Tufail, Y., Yoshihiro, A., Pati, S., Li, M.M., Tyler, W.J., 2011. Ultrasonic neuromodulation by brain stimulation with transcranial ultrasound. Nat. Protoc. 6, 1453–1470. https://doi.org/10.1038/nprot.2011.371

Van Essen, D.C., 2002. Surface-Based Atlases of Cerebellar Cortex in the Human, Macaque, and Mouse. Ann. N. Y. Acad. Sci. 978, 468–479. https://doi.org/10.1111/j.1749-6632.2002.tb07588.x

Van Essen, D.C., Dierker, D.L., 2007. Surface-Based and Probabilistic Atlases of Primate Cerebral Cortex. Neuron 56, 209–225. https://doi.org/10.1016/j.neuron.2007.10.015

Vanduffel, W., 2016. In-Vivo Connectivity in Monkeys, in: Micro-, Meso- and Macro-Connectomics of the Brain, Research and Perspectives in Neurosciences. Springer, Cham, pp. 75–87. https://doi.org/10.1007/978-3-319-27777-6_6

Verhagen, L., 2012. How to grasp a ripe tomato. Utrecht University; Donders Institute, Radboud University.

Vincent, J.L., Patel, G.H., Fox, M.D., Snyder, A.Z., Baker, J.T., Van Essen, D.C., Zempel, J.M., Snyder, L.H., Corbetta, M., Raichle, M.E., 2007. Intrinsic functional architecture in the anaesthetized monkey brain. Nature 447, 83–86. https://doi.org/10.1038/nature05758

Wang, H., Kim, M., Normoyle, K.P., Llano, D., 2016. Thermal Regulation of the Brain—An Anatomical and Physiological Review for Clinical Neuroscientists. Front. Neurosci. 9. https://doi.org/10.3389/fnins.2015.00528

Wattiez, N., Constans, C., Deffieux, T., Daye, P.M., Tanter, M., Aubry, J.-F., Pouget, P., 2017. Transcranial ultrasonic stimulation modulates single-neuron discharge in macaques performing an antisaccade task. Brain Stimulat. 10, 1024–1031. https://doi.org/10.1016/j.brs.2017.07.007

Wise, S.P., 2008. Forward frontal fields: phylogeny and fundamental function. Trends Neurosci. 31, 599–608. https://doi.org/10.1016/j.tins.2008.08.008

Xu, S., Zong, Y., Feng, Y., Liu, R., Liu, X., Hu, Y., Han, S., Wan, M., 2015. Dependence of pulsed focused ultrasound induced thrombolysis on duty cycle and cavitation bubble size distribution. Ultrason. Sonochem. 22, 160–166. https://doi.org/10.1016/j.ultsonch.2014.06.024

Yizhar, O., Fenno, L.E., Davidson, T.J., Mogri, M., Deisseroth, K., 2011. Optogenetics in Neural Systems. Neuron 71, 9–34. https://doi.org/10.1016/j.neuron.2011.06.004

Yoo, S.-S., Bystritsky, A., Lee, J.-H., Zhang, Y., Fischer, K., Min, B.-K., McDannold, N.J., Pascual-Leone, A., Jolesz, F.A., 2011. Focused ultrasound modulates region-specific

brain activity. NeuroImage 56, 1267–1275. https://doi.org/10.1016/j.neuroimage.2011.02.058

Younan, Y., Deffieux, T., Larrat, B., Fink, M., Tanter, M., Aubry, J.-F., 2013. Influence of the pressure field distribution in transcranial ultrasonic neurostimulation. Med. Phys. 40, 082902. https://doi.org/10.1118/1.4812423

Zhang, Y., Aubry, J.-F., Zhang, J., Wang, Y., Roy, J., Mata, J.F., Miller, W., Dumont, E., Xie, M., Lee, K., Zuo, Z., Wintermark, M., 2015. Defining the Optimal Age for Focal Lesioning in a Rat Model of Transcranial HIFU. Ultrasound Med. Biol. 41, 449–455. https://doi.org/10.1016/j.ultrasmedbio.2014.09.029

Zhang, Y., Brady, M., Smith, S., 2001. Segmentation of brain MR images through a hidden Markov random field model and the expectation-maximization algorithm. IEEE Trans. Med. Imaging 20, 45–57. https://doi.org/10.1109/42.906424

Zimmermann, M., Verhagen, L., Lange, F.P. de, Toni, I., 2016. The Extrastriate Body Area Computes Desired Goal States during Action Planning. eNeuro 3, ENEURO.0020-16.2016. https://doi.org/10.1523/ENEURO.0020-16.2016

Figures

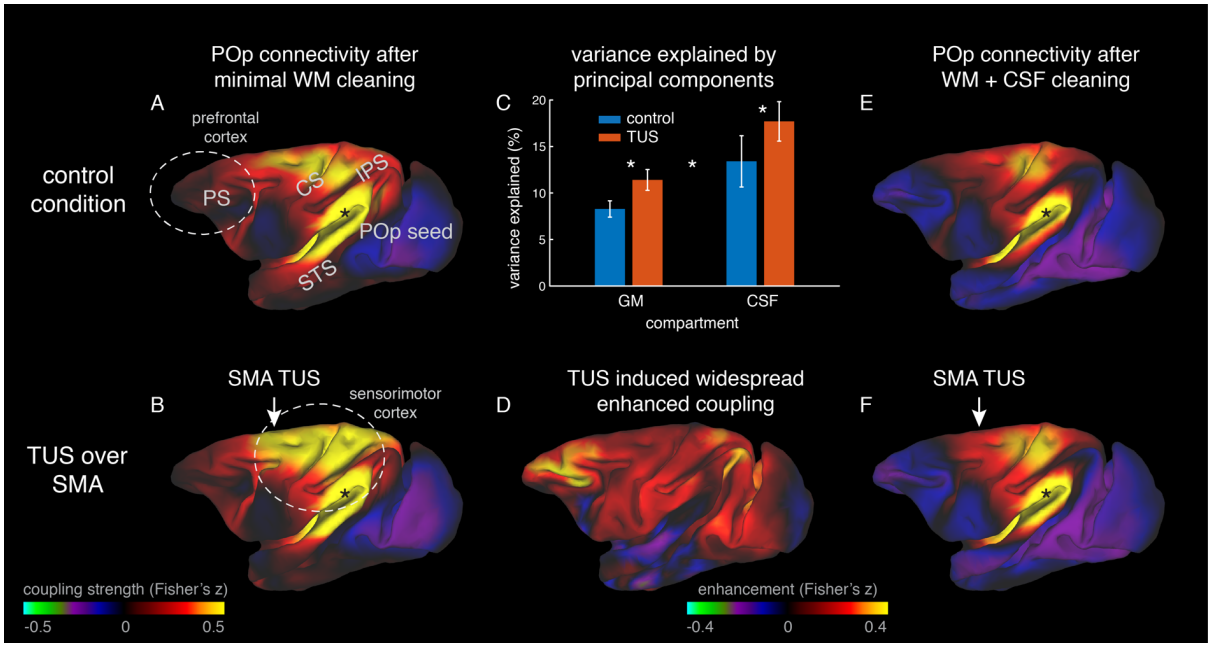

Figure 1. Widespread signal enhancement may have a non-neuronal origin. TUS induced a widespread change in BOLD signal that was not specific to the stimulated area. (**A**) For example, at rest the BOLD signal in the parietal operculum area (POp) was coupled with that in many other areas (positive coupling represented in warm colors from red to yellow). (**B**) POp's functional connectivity pattern became stronger after TUS was applied to a distant area – the SMA. This was because SMA TUS induced broad changes in BOLD signal even in CSF, captured in a principal component analysis (**C**). Error bars denote standard-error of the mean; asterisks denote effects of TUS and WM/CSF compartment ($p < 0.05$). (**D**) This led to many points in the cortex exhibiting stronger coupling with other brain areas; all areas shown in red are points that have stronger coupling with the rest of the brain after TUS. Note that this effect spread far beyond the stimulation site. After cleaning the gray matter signal time course by regressing out the mean time course and the first five principal components of the white matter and CSF signals, POp functional coupling matched its known anatomical connections (**E**) and SMA TUS no longer induced changes in POp connectivity (**F**). Key regions of change are highlighted by white dashed ovals. TUS target sites are indicated with arrows. Connectivity seed regions are indicated with a black asterisk. Key anatomical features are labelled in panel (A): PS, principal sulcus; CS, central sulcus; IPS, intraparietal sulcus; STS, superior temporal sulcus. See also Figure S1.

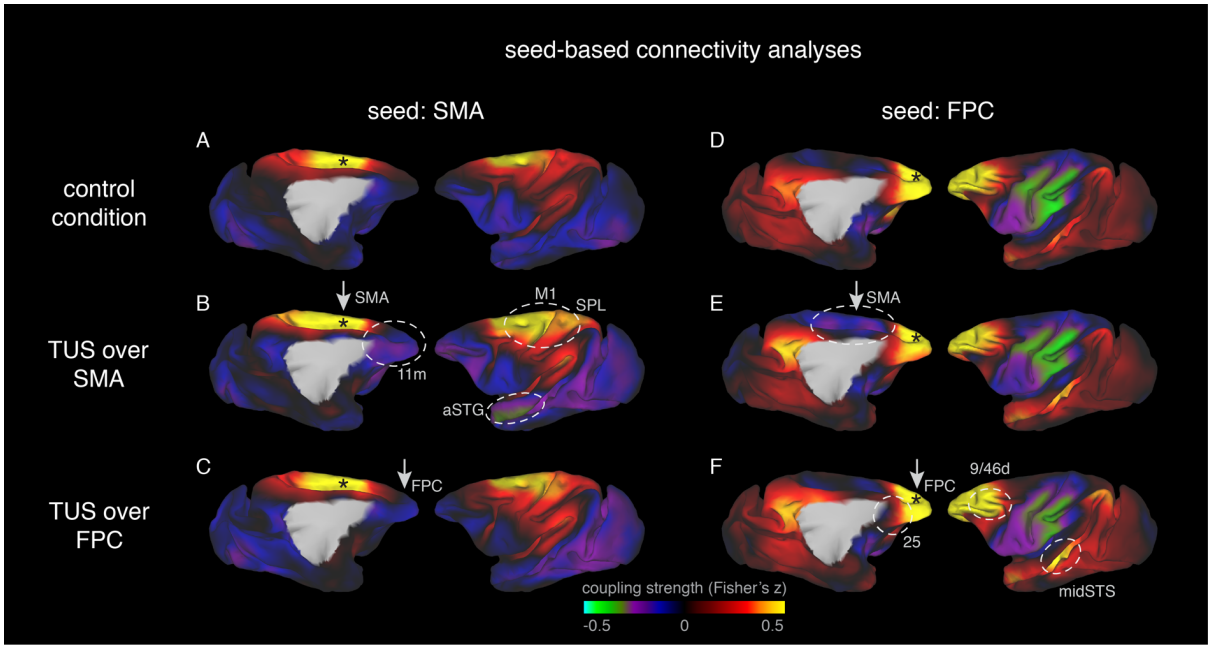

Figure 2. Coupling of activity between stimulated areas and the rest of the brain in experiments 1 and 2. Panels A, B, and C on the left side of the figure show activity coupling between SMA and the rest of the brain in control animals (**A**), after SMA TUS (**B**), and after FPC TUS (**C**). Panels D, E, F on the right show activity coupling between FPC and the rest of the brain in control animals (**D**), after SMA TUS (**E**), and after FPC TUS (**F**). Functional connectivity from TUS-targeted regions is therefore summarized in panels b and f (i.e. SMA connectivity after SMA TUS and FPC connectivity after FPC TUS). Each type of TUS had a relatively selective effect on the stimulated area: SMA coupling was changed by SMA TUS (**B**) and FPC coupling was changed by FPC TUS (**F**). All other conventions as in Figure 1. See also Figure S2.

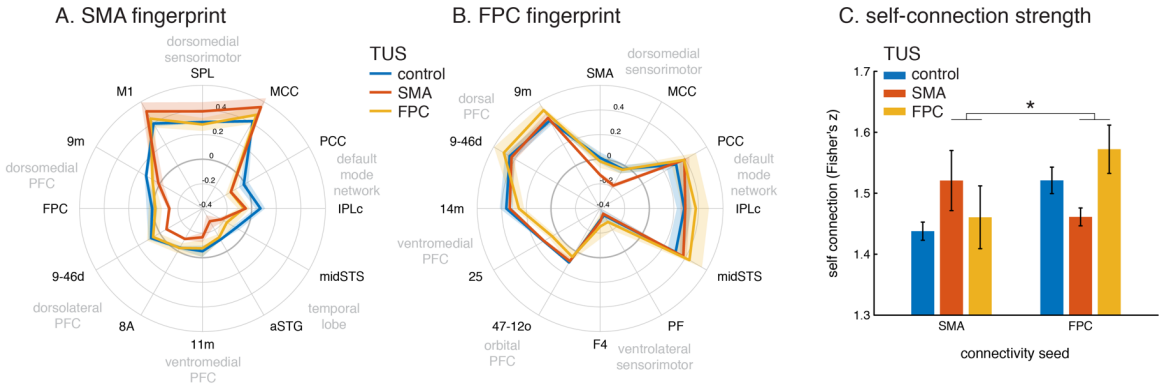

Figure 3. Connectional fingerprints of the stimulated areas. The effect of TUS can also be illustrated by examining each region's connectivity fingerprint after stimulation is applied to it, to the other region, and in the control state. (**A**) The blue line indicates the strength of activity coupling between SMA and each of the brain regions shown on the circumference of the panel. These fingerprint target regions were drawn from the literature and chosen based on their known and distinct connectivity, either strong or weak, with the seed region. It shows that in the control state SMA is strongly coupled to areas in the dorsomedial sensorimotor system (M1, SPL, MCC). Coupling with each of these areas is enhanced after SMA TUS (red). In contrast, coupling with prefrontal (9m, FPC, 9-46d, 8A, 11m), temporal (aSTG, midSTS), and parietal (IPLc, PCC) regions that SMA is weakly connected with in the control state are even further reduced after SMA TUS (red). However, SMA's fingerprint is relatively unaffected after FPC TUS (yellow), but some effects are visible for regions that are strongly coupled with FPC (compare to panel b). (**B**) The blue line indicates the strength of activity coupling between FPC and each of the brain regions shown on the circumference of the panel in the control state, revealing strong coupling to dorsal prefrontal areas 9-46d and 9m, and the temporo-parietal default mode network (midSTS, IPLc, PCC). Coupling with each of these areas is increased after FPC TUS while FPC coupling with other areas is disrupted (yellow). However, FPC's coupling with other brain areas is relatively unaffected after SMA TUS, with the exception of SMA itself and the strongly connected MCC (red). Thick blue, red, and yellow lines indicate mean activity coupling effect in the control state, after SMA TUS, and after FPC TUS, respectively (within subjects, n=3). In each case the lighter colored error bands indicate the standard-error of the mean across individual animals. (**C**) TUS tended to induce increased coupling in activity within the stimulated area (red on the left, yellow on the right) but decreased coupling with activity in more distantly located and more weakly interconnected

areas (yellow on the left, red on the right). This is apparent in the way that FPC TUS led to increased coupling within FPC itself but not between FPC and other areas (left) while SMA TUS led to increased coupling between points within SMA but not between SMA and FPC. Error bars depict standard-error of the mean; asterisk denotes the interaction between TUS site and connectivity seed ($p < 0.001$). See also Figure S2 and Figure S3.

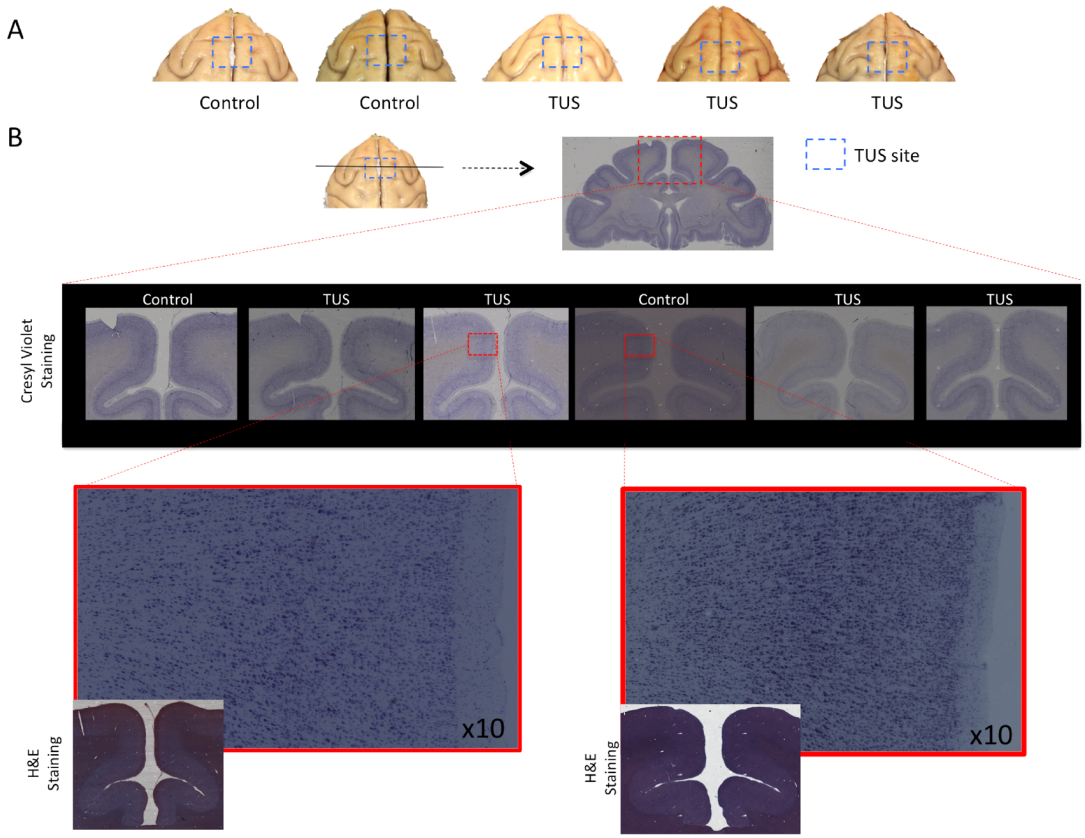

Figure 4. No effect of TUS was apparent on histological examination. (**A**) Dorsal view of perfused macaque brain. A post-mortem examination of the brain did not reveal macroscopic damage to the brain. (**B**) Histological assessment of 50 micron thick sections obtained at the level of the stimulation site with Cresyl Violet Nissl staining and H&E staining did not reveal any evidence of thermal lesions or hemorrhage after the TUS protocol used here. Magnified images are centered at the focal point of the stimulation, where acoustic energy is expected to be maximal.

Methods

Contact details

Please direct any inquiries, resource requests, or software requests to the Lead Contact, Lennart Verhagen (lennart.verhagen@psy.ox.ac.uk, @LennartVerhagen).

Experimental model and subject details

For this study, six healthy male macaques (*Macaca mulatta*) were stimulated with transcranial focused ultrasound and scanned to acquire resting state functional magnetic resonance (rs-fMRI) and anatomical MR images. Three animals participated in experiments 1 and 2, including the control condition (mean age and weight at time of scan: control, 5.5 years, 10.2 kg; SMA TUS, 5.6 years, 10.7 kg; FPC TUS, 6.1 years, 11.8 kg). Three different animals participated in experiment 3 (mean age and weight at time of scan: 10.3 years, 13 kg). In addition to this set of animals, six animals were included in the histology analysis (experiment 4): three control animals who did not receive TUS (2 females; mean age and weight at time of perfusion: 9.3 years, 9.1 kg) and three pre-SMA TUS animals post stimulation (3 males; mean age and weight at time of perfusion: 8.4 years, 13.1 kg).

All procedures were conducted under licenses from the United Kingdom (UK) Home Office in accordance with The Animals (Scientific Procedures) Act 1986. In all cases they complied with the European Union guidelines (EU Directive 2010/63/EU).

Method details

Ultrasound stimulation

A single element ultrasound transducer (H115-MR, diameter 64 mm, Sonic Concept, Bothell, WA, USA) with 51.74 mm focal depth was used with a coupling cone filled with degassed water and sealed with a latex membrane (Durex). The resonance frequency of ultrasonic wave was set at 250 kHz with 30 ms bursts of ultrasound generated every 100 ms, controlled through a digital function generator (Handyscope HS5, TiePie engineering, Sneek, The Netherlands). The stimulation lasted for 40 seconds. A 75-Watt amplifier (75A250A, Amplifier Research, Souderton, PA) was used to deliver the required power to the transducer. A TiePie

probe (Handyscope HS5, TiePie engineering, Sneek, The Netherlands) connected to an oscilloscope was used to monitor the voltage delivered. The recorded peak-to-peak voltage was constantly maintained at 130V and corresponded to a peak negative pressure of 1.2MPa measured in water with an in house heterodyne interferometer (Constans et al., 2017). Based on a mean 66% transmission through the skull (Wattiez et al., 2017), the estimated peak negative pressures applied are 0.84 MPa at the target in the brain. Each of the areas targeted in experiments 1-4 lie close to the midline. Therefore, we applied a single train over the midline stimulating the target region in both hemispheres simultaneously.

In order to direct TUS to the target region, we guided the stimulation using a frameless stereotaxic neuronavigation system (Rogue Research, Montreal, CA) set up for each animal individually by registering a T1-weighted MR image to the animal's head. Positions of both the ultrasound transducer and the head of the animal were tracked continuously with infrared reflectors to inform online and accurate positioning of the transducer over the targeted brain region: SMA in experiment 1, (Montreal Neurological Institute (MNI) X, Y, and Z coordinates in mm [0.1 2 19]); FPC in experiment 2 [0.6 24 10]; FPC in experiment 3 [-0.7 24 11]; pre-SMA in experiment 4 [0.2 11 17]. The ultrasound transducer / coupling cone montage was placed directly onto previously shaved skin prepared with conductive gel (SignaGel Electrode; Parker Laboratories Inc.) to ensure ultrasonic coupling between the transducer and the animal's scalp. In the non-stimulation condition (control), all procedures (anesthesia, pre-scan preparation, fMRI scan acquisition and timing), with the exception of actual TUS, matched the TUS sessions.

Thermal modelling

The propagation of focused ultrasound was simulated in an entire monkey head to obtain the pressure amplitude and spatial distribution at steady state. The simulations were performed using a k-space pseudospectral method-based solver, k-Wave (Cox et al., 2007). 3D maps of the skull, brain, and tissues were extracted from a monkey CT scan (0.36 mm resolution). Soft tissues were assumed to be homogeneous, with acoustic values close to those of water (ρ_{tissue} =1030 kg/m^3 and c_{tissue} =1560 m/s) (Constans et al., 2018). In the bone, a linear relationship between the Hounsfield Units (HU) from the CT scan and the sound speed, as well as the density, was used. The power law model for attenuation is $\alpha_{\mathrm{att}} = \alpha_1 * \Phi^{\beta}$ where the porosity

Φ is defined by $\Phi = \frac{\rho_{max}-\rho}{\rho_{max}-\rho_{water}}$ in the skull (Aubry et al., 2003). The attenuation coefficient for the acoustic propagation α1 depends on the frequency: $\alpha_1 = \alpha_0 f^b$. We set the parameters to $\rho_{max} = 2200\ \mathrm{kg}/m^3, c_{max} = 3100\ m/s, \beta = 0.5, \alpha_0 = 8\ dB/cm/MHz^b$, b=1.1. (Constans et al., 2018). The attenuation coefficient in bone accounts for both absorption and scattering.

The propagation simulation was performed at 250 kHz with a 150µs-long pulse signal (enough to reach a steady state) and a 0.41 mm pixel size. The transducer was modelled as a spherical section (63 mm radius of curvature and 64 mm active diameter). The simulated pulses were spatially apodized (r = 0.35) on the spherical section. Ultrasound propagates first through the water-filled cone before entering the head, since the geometrical focal point is located below the surface, inside the brain. The pressure amplitude map was then rescaled to a maximum pressure of 0.84 MPa in the brain, corresponding to the estimated experimental value.

The thermal modeling is based on the bio-heat equation (Pennes, 1948):

$$\rho C \frac{\partial T}{\partial t} = \kappa \nabla^2 T + q + w \rho_b C_b (T - T_a)$$

where T, ρ, C, κ and q are the temperature, density, specific heat, thermal conductivity and rate of heat production respectively. Heat production is defined as $q = \alpha_{abs} \frac{PPP}{2\rho C}$, α_{abs} being the absorption coefficient. κ is set to 0.528 $W.m^{-1}.K^{-1}$ in soft tissue and 0.4 $W.m^{-1}.K^{-1}$ in the skull; C is set to 3600 $J.kg^{-1}.K^{-1}$ in soft tissue and 1300 $J.kg^{-1}.K^{-1}$ in the skull (Duck, 2013). In the tissue, the absorption coefficient was set to $\alpha_{abs\ tissue} = 0.21\ \mathrm{dB/cm}/MHz^b$ (Goss et al., 1979). In the skull the longitudinal absorption coefficient is proportional to the density with $\alpha_{abs\ max} = \alpha_0/3 = 2.7\ \mathrm{dB/cm}/MHz^b$ (Pinton et al., 2012). The last term corresponds to the perfusion process: w, ρ_b, C_b and T_a correspond to the blood perfusion rate, blood density, blood specific heat and blood ambient temperature respectively. These parameters are assumed homogeneous over the brain, although a more detailed description of the brain cooling processes can be found in the literature (Wang et al., 2016). The perfusion parameters are based on previous reports (Pulkkinen et al., 2011): $w=0.008 s^{-1}$; $\rho_b = 1030\ kg.m^{-3}$; $C_b = 3620\ J.kg^{-1}.K^{-1}$ and $T_a = 37°C$.

The bioheat equation is solved by using a 3D finite-difference scheme in MATLAB (Mathworks, Natick, USA) with Dirichlet boundary conditions. Initial temperature conditions were 37°C in

the brain, skull and tissue, and 24°C in the water coupling cone. Simulations were run over 2 minutes pre-sonication, followed by 40 s of sonication, and 5 minutes post-sonication, closely following the experimental procedure.

Macaque MRI acquisition

MRI scans were collected under inhalational isoflurane anesthesia using a protocol which has previously proven successful in preserving whole-brain functional connectivity as measured with BOLD signal (Mars et al., 2013, 2011; Neubert et al., 2015, 2014; O'Reilly et al., 2013; Sallet et al., 2013; Vincent et al., 2007). In the case of the TUS conditions, fMRI data collection began only after completion of the TUS train. Anesthesia was induced using intramuscular injection of ketamine (10 mg/kg), xylazine (0.125– 0.25 mg/kg), and midazolam (0.1 mg/kg). Macaques also received injections of atropine (0.05 mg/kg, intramuscularly), meloxicam (0.2 mg/kg, intravenously), and ranitidine (0.05 mg/kg, intravenously). The anesthetized animals were placed in an MRI-compatible frame (Crist Instruments) in a sphinx position and placed in a horizontal 3 T MRI scanner with a full-size bore. Scanning commenced ~2 h after induction, when the clinical peak of ketamine had passed. Anesthesia was maintained, in accordance with veterinary recommendation, using the lowest possible concentration of isoflurane to ensure that macaques were anesthetized. The depth of anesthesia was assessed and monitored using physiological parameters (heart rate and blood pressure, as well as clinical checks before the scan for muscle relaxation). During the acquisition of the functional data the expired isoflurane concentration was in the range 0.6-0.8%. Isoflurane was selected for the scans as it was previously demonstrated to preserve rs-fMRI networks (Mars et al., 2013, 2011; Neubert et al., 2015, 2014; O'Reilly et al., 2013; Sallet et al., 2013; Vincent et al., 2007). Macaques were maintained with intermittent positive pressure ventilation to ensure a constant respiration rate during the functional scan, and respiration rate, inspired and expired CO2, and inspired and expired isoflurane concentration were monitored and recorded using VitalMonitor software (Vetronic Services Ltd.). Core temperature and SpO2 were also constantly monitored throughout the scan. A four-channel phased-array coil was used for data acquisition (Dr. H. Kolster, Windmiller Kolster Scientific, Fresno, CA, USA).

FMRI data were collected in experiments 1-3. Whole-brain BOLD fMRI data were collected from each animal for 3 runs of approximately 26 minutes each, using the following

parameters: 36 axial slices; in-plane resolution, 2 x 2 mm; slice thickness, 2 mm; no slice gap; TR, 2000 ms; TE, 19 ms; 800 volumes per run. A minimum period of 10 days elapsed between sessions.

T1-weighted structural MRI scans were collected in experiments 1-3. A structural scan (average over up to three T1w images acquired in the same session) was acquired for each macaque in the same session, using a T1 weighted magnetization-prepared rapid-acquisition gradient echo sequence (0.5 x 0.5 x 0.5 mm voxel resolution).

Macaque anatomical MRI preprocessing

The preprocessing and analysis of the MRI data was designed to follow the HCP Minimal Processing Pipeline (Glasser et al., 2013), using tools of FSL (https://fsl.fmrib.ox.ac.uk/fsl/fslwiki), HCP Workbench (https://www.humanconnectome.org/software/connectome-workbench), and the Magnetic Resonance Comparative Anatomy Toolbox (MrCat; http://www.rbmars.dds.nl/lab/toolbox.html). The T1w images were processed in an iterative fashion cycling through brain-extraction, RF bias-field correction, and linear and non-linear template registration to the *macaca mulatta* F99 atlas (Van Essen, 2002; Van Essen and Dierker, 2007). The initial skull stripping was performed using a multi-seeded implementation of BET (Smith, 2002) optimized for macaque brains, while subsequent brain extraction was based on a high-fidelity template registered to the F99 macaque space. The RF bias-field was estimated and corrected using a robust implementation of FAST (Zhang et al., 2001). Linear and non-linear registration to F99 space was achieved using FLIRT (Jenkinson et al., 2002; Jenkinson and Smith, 2001) and FNIRT (Andersson et al., 2007; Jenkinson et al., 2012) with configurations adjusted to reflect macaque rather than human brain characteristics. The application of a robust and macaque-optimised version of FAST also resulted in compartments estimated for grey matter, white matter, and cerebral spinal fluid. For each compartment a posterior-probability map was created by integrating a set of prior probability maps based on 112 *Macaca mullata* individuals (McLaren et al., 2009) with the dataset-specific evidence provided by FAST. Segmentation of subcortical structures was achieved by registration to the D99 atlas (Reveley et al., 2017).

Macaque rs-fMRI preprocessing

The first 5 volumes of the functional EPI datasets were discarded to ensure a steady RF excitation state. EPI timeseries were motion corrected using MCFLIRT. Given that the animals were anesthetized and their heads were held in a steady position, any apparent image motion, if present at all, is caused by changes to the B0 field, rather than by head motion. Accordingly, the parameter estimates from MCFLIRT can be considered to be 'B0-confound parameters' instead. Each timeseries was checked rigorously for spikes and other artefacts, both visually and using automated algorithms; where applicable slices with spikes were linearly interpolated based on temporally neighboring slices. Brain extraction, bias-correction, and registration was achieved for the functional EPI datasets in an iterative manner, similar to the preprocessing of the structural images with the only difference that the mean of each functional dataset was registered to its corresponding T1w image using rigid-body boundary-based registration (FLIRT). EPI signal noise was reduced both in the frequency and temporal domain. The functional time series were high-pass filtered with a frequency cut-off at 2000 seconds. Temporally cyclical noise, for example originating from the respiration apparatus, was removed using band-stop filters set dynamically to noise peaks in the frequency domain of the first three principal components of the timeseries.

For the minimally processed data (figs 1, S1), remaining temporal noise was described by the mean time course and the first five subsequent principal components of the white matter (WM) compartment (considering only voxels with a high posterior probability of belonging to the WM, obtained in the T1w image using FAST). The principal components of the WM signal were estimated using a singular value decomposition approach. The B0 confound parameter estimates obtained from MCFLIRT were expanded as a second degree Volterra series to capture both linear and non-linear B0 effects. Together the WM and expanded B0 confound parameters were regressed out of the BOLD signal for each voxel.

For the fully processed data (figs 2, 3, S2, S3), the confound cleaning was identical to the minimally processed data, including the number of compartment components (6 in total) and the Volterra expansion of the B0 confound parameters, except for the mask from which the compartment components were derived. Namely, for these data the mask encompassed not only high-probability WM but also high-probability cerebral spinal fluid (CSF) voxels.

For both types of analyses, after this confound cleaning step, the time course was low-pass filtered with a cut-off at 10 seconds. The cleaned and filtered signal was projected from the conventional volumetric representation (2 mm voxels) to the F99 cortical surface (~1.4

mm spaced vertices), while maintaining the subcortical volumetric structures. The data was spatially smoothed using a 3 mm FWHM gaussian kernel, taking into account the folding of the cortex and the anatomical boundaries of the subcortical structures. Lastly, the data were demeaned to prepare for functional connectivity analyses.

To represent subject effects, the timeseries from the three runs were concatenated to create a single timeseries per animal per intervention (control, SMA TUS, FPC TUS). To represent group effects the run-concatenated timeseries of all animals were combined using a group-PCA approach (Smith et al., 2014) that was set to reduce the dimensionality of the data.

Quantification and statistical analysis

Macaque rs-fMRI connectivity analysis

To construct regions-of-interest (ROI) for SMA and FPC circles of 4 mm radius were drawn on the cortical surface around the point closest to the average stimulation coordinate (fig S4), in both the left and the right hemisphere. The same procedure was used to define other bilateral cortical regions of interest, based on literature coordinates (Mars et al., 2011; Neubert et al., 2015, 2014; Sallet et al., 2013), to serve as seeds for connectivity analyses (POp, fig 1) or targets for the fingerprint analyses (fig 3). Apart from the stimulation sites, all ROIs were selected based on their known anatomical connectivity, of relevance because they are known to be distinctively strongly or distinctively weakly connected with the stimulation sites.

Coupling between the activity of each region of interest and the rest of the brain was estimated by calculating the Fisher's z-transformed correlation coefficient between each point in the ROI and all other data points. The resulting "connectivity-maps" were averaged across all vertices/voxels in the ROI, and subsequently averaged across hemispheres. Accordingly, the final maps represent the average coupling of a bilateral ROI with the rest of the brain. The fingerprints are obtained by extracting the average coupling with each target ROI and averaging across the two hemispheres.

Macaque rs-fMRI statistical inference

No data was excluded for analysis. Statistical inference on the fingerprints was performed by using non-parametric permutation tests on cosine similarity metrics describing how similar or

dissimilar pairs of fingerprints are (Mars et al., 2016). In contrast to conventional parametric tests, this approach does not rely on assumptions about the shape of the distribution but will acknowledge dependencies between target ROIs in the fingerprint; as such this approach will avoid inflation of type I error. The relatively small number of TUS sites, animals, and fMRI runs allowed us to exhaustively test all possible permutations (24309) to obtain the true probability of rejecting the null hypothesis. The center of data across individual animals is derived directly from the group-PCA approach (Smith et al., 2014) where all animals (n=3) received equal wait. Dispersion is described as the standard-error of the mean across the individual animals (n=3).

All other statistical inferences were drawn in the context of generalized linear mixed-effects (GLME) models that considered the intercept and factorial design (including interactions where appropriate) as fixed effects and the intercept and slope grouped per animal as random effects with possible correlation between them (as implemented in MATLAB, Mathworks, Natick, USA). The models assumed a normal distribution of the data and were fitted using Maximum-Pseudo-Likelihood estimation methods where the covariance of the random effects was approximated using Cholesky parameterization. Statistical significance was set at $\alpha = 0.05$, two-tailed.

We described the signal variance in the GM and CSF compartments, or more specifically, the variance explained by the first five principal components (figs 1c, S1d), using the same approach that was used to decompose signal in WM or WM+CSF compartments in the EPI timeseries cleaning step, as described above. We defined the explained variance as the sum of the first five eigenvalues of the covariance matrix of the compartment signals divided by the sum of all eigenvalues. Statistical inference was drawn using GLME models that considered the effects of compartment and TUS intervention.

In minimally processed data, which did not consider the CSF compartment in the data cleaning step, we quantified the effect of TUS for each point on the cortical surface. For each point, we calculated it's coupling with the rest of the brain, sorted all Fisher's z-values in ascending order, and extracted the z-value at the 98th-percentile. Z-values at this level describe relatively strong coupling with the seed point and are often observed in the vicinity of the seed region or other strongly connected regions (depicted in bright yellow in figure 1), ensuring that irrelevant connections are ignored. As such, this simple statistic is well-suited to capture any main effects of TUS on coupling strength, including those observed when

comparing panels (a) and (b) in figure 1. This statistic allows us to quantify the effect of TUS in a single value for each point on the cortical surface, and to directly contrast the values obtained in the control state with those obtained after TUS (figs 1d, S1e, f).

The strength of self-connections within SMA and FPC ROIs was estimated in the same way as the coupling of either SMA or FPC with any remote ROI was determined. Namely, for each point in the ROI the Fisher's z-transformed correlation between this point's timeseries and that of each of the other points in the ROI was calculated. Subsequently, for each point the resultant z-values were averaged, describing local coupling at that point, and averaged across the whole ROI to obtain a single estimate of self-coupling per ROI (fig 3c). Statistical inference was drawn using GLME models that considered the effects of connectivity ROI (SMA, FPC) and TUS site (SMA, FPC).

Histology

In experiment 4, prior to histological examination, animals were anesthetized with sodium pentorbarbitone and perfused with 90% saline and 10% formalin. A post-mortem examination of the surface of the brain was conducted prior to the brain extraction. The brains were then removed and placed in 10% sucrose formalin. The brains were blocked in the coronal plane at the level of the lunate sulcus. Each brain was cut in 50-µm coronal sections. Every tenth section, two adjacent sections were retained for analysis whereby one was stained with Cresyl Violet (Nissl body staining) and the other with Haemotoxylin and Eosin (H&E staining).

Data and software availability

FSL can be downloaded from https://fsl.fmrib.ox.ac.uk/fsl/fslwiki. HCP Workbench can be downloaded from https://www.humanconnectome.org/software/connectome-workbench. For any information regarding MrCat please see http://www.rbmars.dds.nl/lab/toolbox.html, further inquiries can be directed to Lennart Verhagen (lennart.verhagen@psy.ox.ac.uk) or Rogier Mars (rogier.mars@ndcn.ox.ac.uk). All dedicated software tools will be made available at https://github.com/neuroecology/MrCat. For any inquiries regarding the data, please contact Jérôme Sallet (jerome.sallet@psy.ox.ac.uk).

Supplemental Information

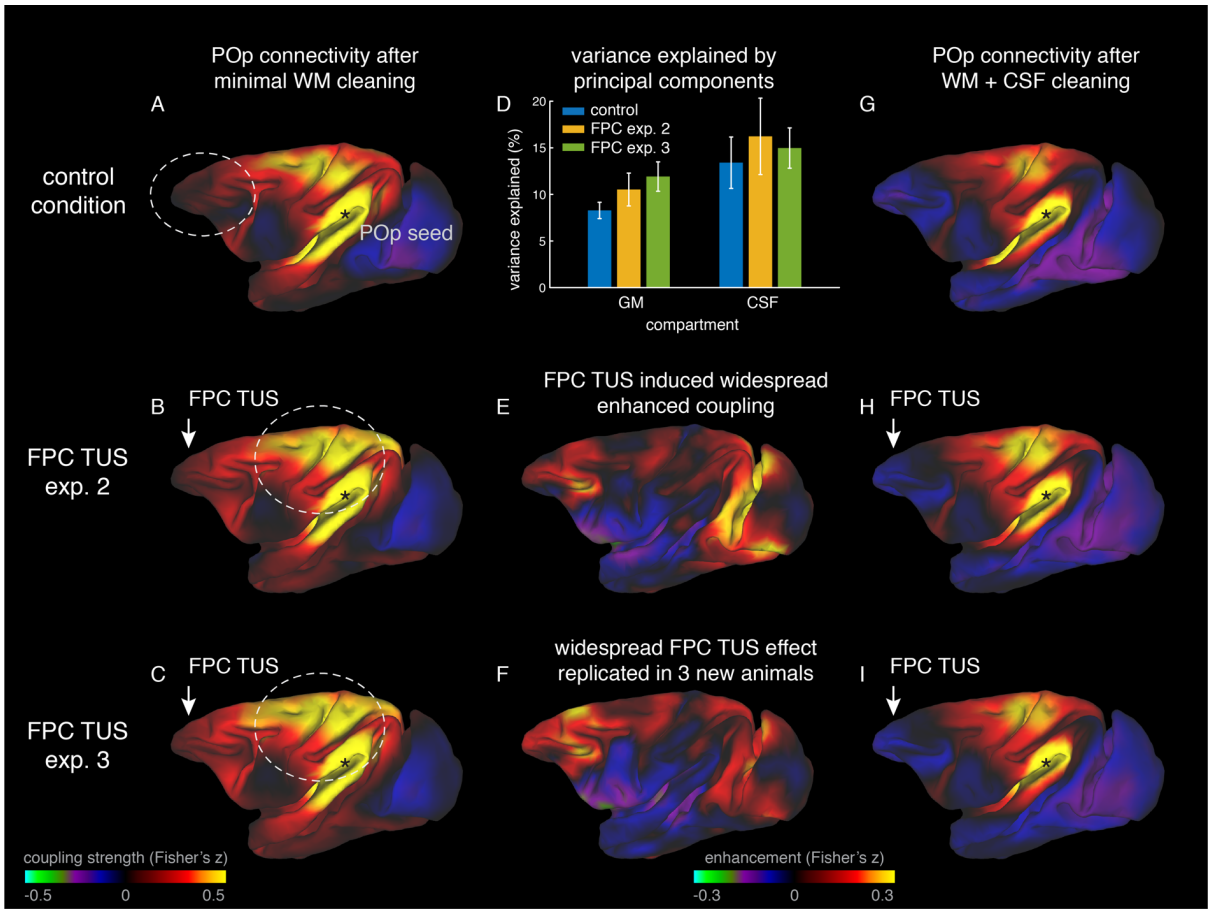

Figure S1. Related to Figure 1. Widespread signal enhancements were replicated in experiments 2 and 3. TUS induced similar widespread changes in BOLD signal that were not specific to the stimulated area, FPC, in experiments 2 and 3. (**A**) For example, at rest the BOLD signal in the parietal operculum area (POp) was coupled with that in many other areas (positive coupling represented in warm colors from red to yellow). (**B**) POp's functional connectivity pattern became stronger after TUS was applied to FPC in experiment 2. Similar effects were again seen in experiment 3 (**C**). This was because FPC TUS induced broad changes in BOLD signal even in CSF, captured in a principal component analysis in both experiments 2 and 3 (**D**). This led to many points in the cortex exhibiting stronger coupling with other brain areas in both experiments 2 (**E**) and 3 (**F**); all areas shown in red are points that have stronger coupling with the rest of the brain after TUS. (**G**) After cleaning the gray matter signal time course by regressing out the mean time course and the first five principal components of the white matter and CSF signals, FPC TUS no longer induced changes in POp connectivity in both experiments 2 (**H**) and 3 (**I**). Panels (A) and (G) are reproduced here from Figure 1 for comparison. All other conventions as in Figure 1. Error bars depict standard-error of the mean.

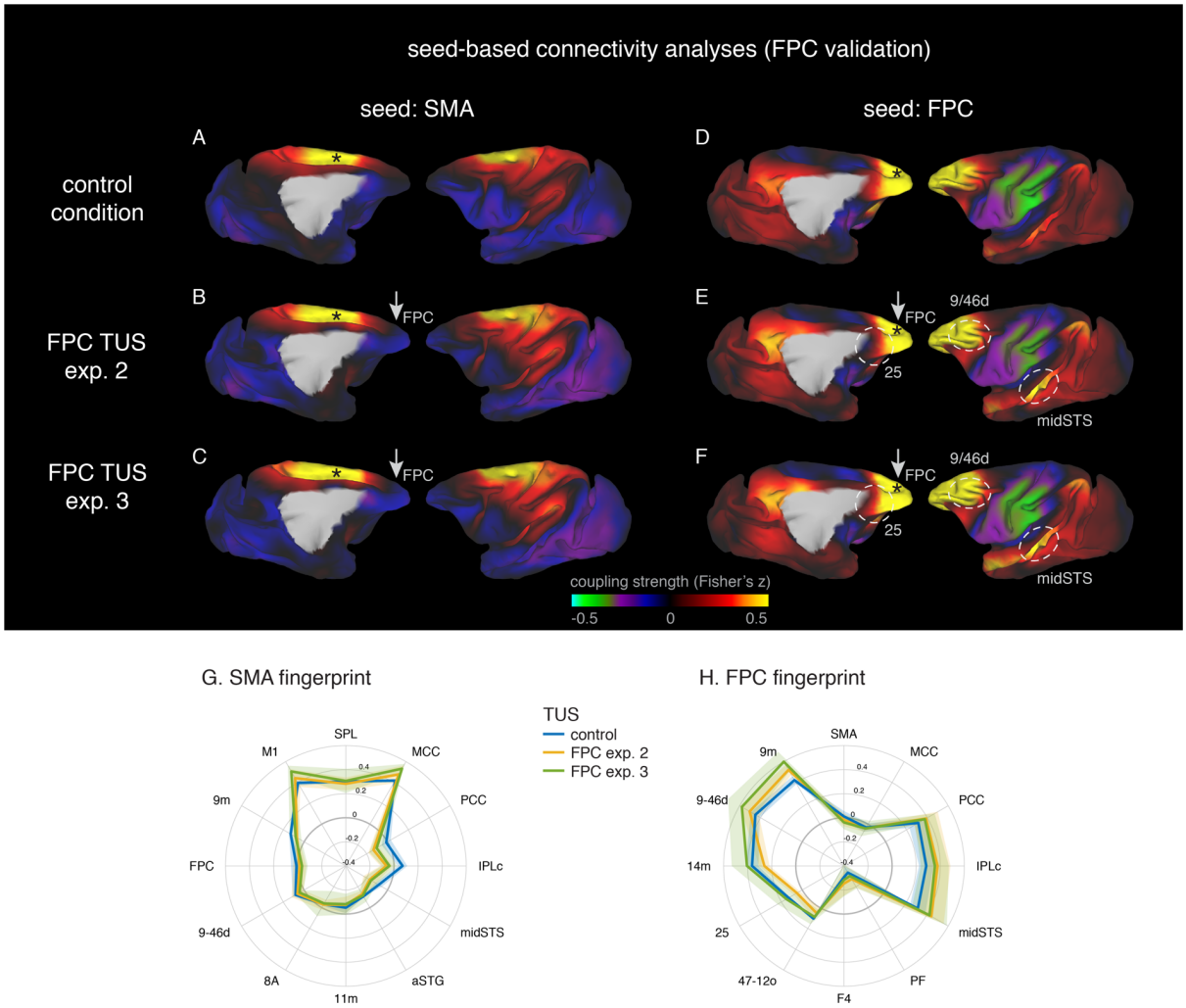

Figure S2. Related to Figures 2 and 3. Specific patterns of change in the coupling of activity between stimulated areas and the rest of the brain were replicated in experiments 2 and 3. Panels a, b, and c on the left side of the figure show activity coupling between SMA and the rest of the brain in control animals (**A**), after FPC TUS in experiment 2 (**B**), and after FPC TUS in experiment 3 (**C**). Panels d, e, f on the right show activity coupling between FPC and the rest of the brain in control animals (**D**), after FPC TUS in experiment 2 (**E**), and after FPC TUS in experiment 3 (**F**). SMA's connectional fingerprint was largely unaltered after FPC TUS in both experiments 2 and 3 (**G**) but FPC's connectivity fingerprint was altered in a similar manner in both experiments 2 and 3 (**H**). Panels (A, B) and (D, E) are reproduced here from Figure 2 for comparison. All other conventions as in Figure 2. Lighter colored error bands indicate the standard-error of the mean across individual animals.

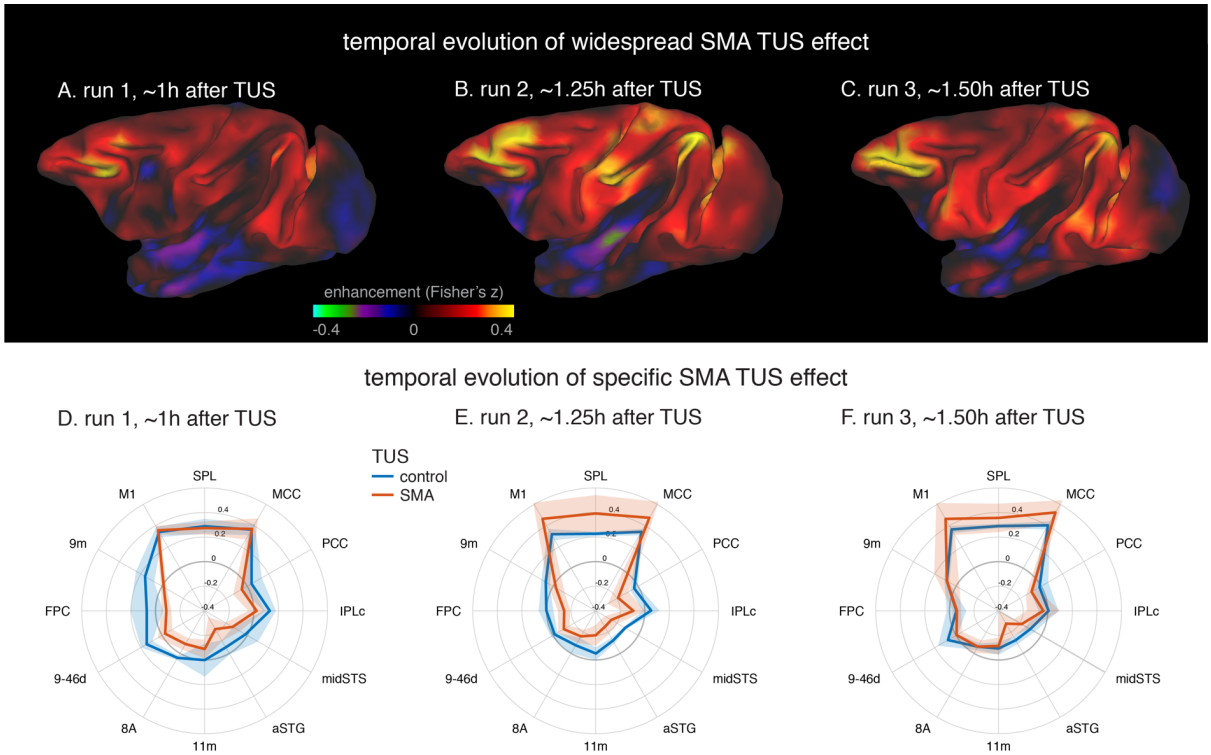

Figure S3. Related to Figures 1 and 3. Persistence and temporal evolution of TUS effects. Both the global, non-specific effects of TUS persisted over time (**A-C**) as did the spatially specific effects that can be illustrated in the connectional fingerprint of SMA (**D-F**). The left panels depict effects observed in the first fMRI run, followed by the second run in the middle, and the third and last run on the right. For each run, the time after TUS refers to the duration between the end of TUS and the midpoint of the run, averaged across the 3 animals. Lighter colored error bands indicate the standard-error of the mean across individual animals.

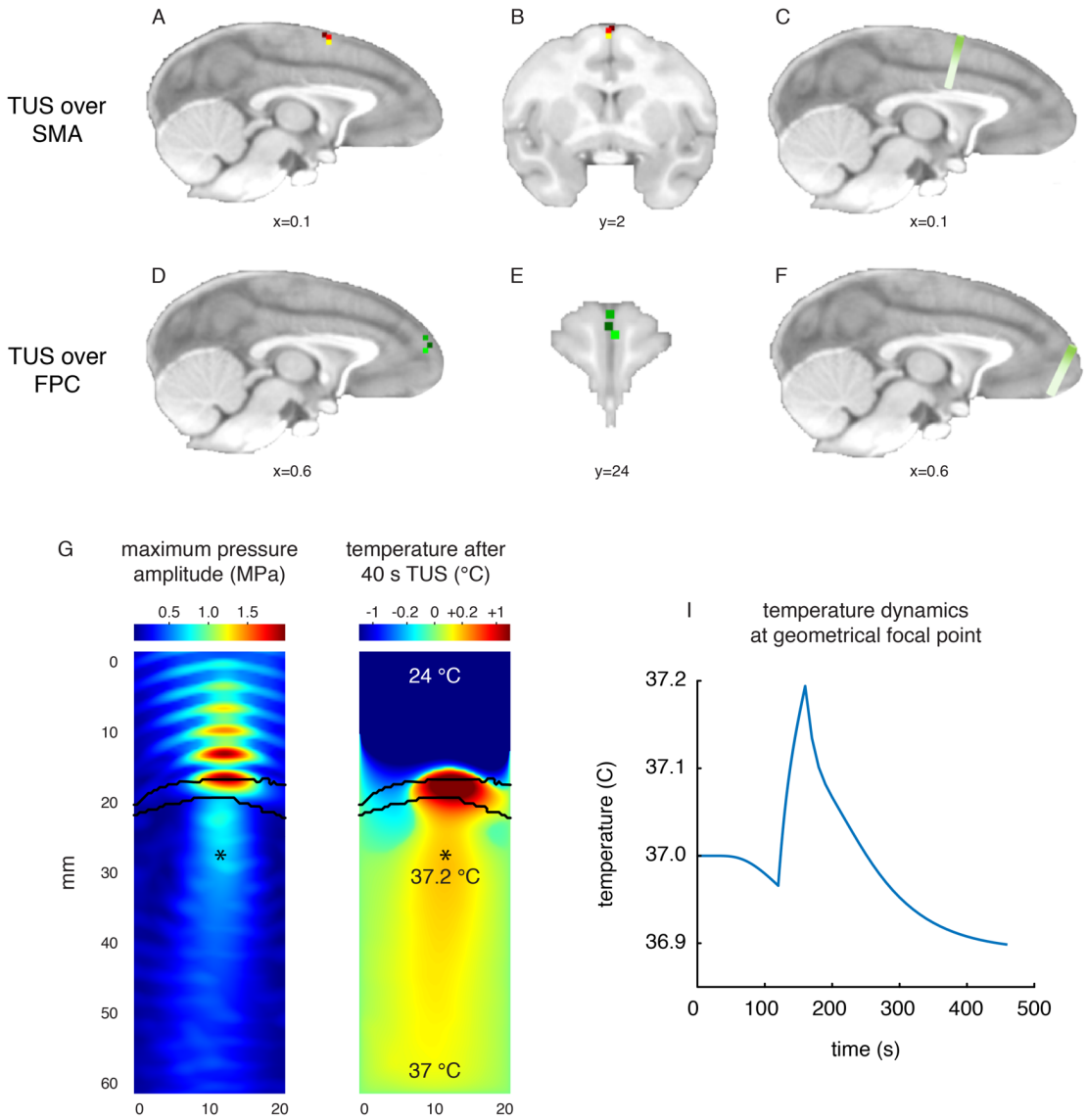

Figure S4. Related to Figures 1, 2, and 3. Stimulation targets and thermal modelling. Stimulation target position is shown in each of three individual animals in three different colors in SMA on sagittal (**A**) and coronal views (**B**). The trajectory of stimulation is shown in one example animal (**C**). FPC targets in three animals are shown on sagittal (**D**) and coronal sections (**E**) and the stimulation trajectory is shown for one animal (**F**). Whole head simulations of the acoustic wave and thermal dynamics provided estimates of the maximum pressure amplitude (**G**, left panel) and the temperature after 40 s TUS (**G**, right panel). Panels (G) depicts a cropped plane of the whole-head simulations with the sonic coupling cone at the top, above the skull in black outlines, and the brain on the bottom with the geometrical focal point indicated with asterisk. Pressure and temperature are maximal in the skull, which is more absorbing than soft tissue. Temperature changes are represented on a symmetrical square-root scale to highlight the small temperature changes inside the brain. (**I**) Temperature dynamics at the geometrical focal point in the cortex.